

MICROELASTOHYDRODYNAMICS OF SWIMMING ORGANISMS NEAR SOLID BOUNDARIES IN COMPLEX FLUIDS

by N. J. BALMFORTH[†]

(Department of Mathematics and Institute of Applied Mathematics, University of British Columbia, 1984 Mathematics Road, Vancouver, British Columbia V6T 1Z2, Canada and Department of Earth and Ocean Science, University of British Columbia, 6339 Stores Road, Vancouver, British Columbia V6T 1Z4, Canada)

and

D. COOMBS and S. PACHMANN

(Department of Mathematics and Institute of Applied Mathematics, University of British Columbia, 1984 Mathematics Road, Vancouver, British Columbia V6T 1Z2, Canada)

[Received 18 August 2009. Revised 27 April 2010. Accepted 4 May 2010]

Summary

Microorganisms such as sperm routinely swim close to solid boundaries and within non-Newtonian fluids. In this paper, we exploit the lubrication approximation to model the motion of a flexible sheet near a rigid wall and immersed in a complex fluid. This allows us to specify an internally generated force density on the sheet and allow its shape and velocity to be determined by the interplay between the forcing and the fluid motion. We obtain results for Newtonian and complex fluids, focusing specifically on the influence of shear thinning/thickening and of yield stress. In the latter case, we characterise the threshold forcing that is required for successful swimming to occur. Our results highlight the usefulness of the lubrication approach in modelling micro-scale fluid–structure interactions.

1. Introduction

In a seminal 1951 paper, Taylor (1) proposed a simple fluid mechanical model for the swimming of a microorganism. He modelled the organism as an infinite flexible sheet suspended in a viscous fluid. The organism was assumed to be able to send transverse waves along its length to propel itself forward. By considering the zero Reynolds number limit and taking the propulsive waves to be sinusoidal and of low amplitude, he was able to solve the problem analytically and establish formulae for the swimming speed in terms of the wave amplitude. Taylor's article prompted a great many studies that followed on and generalised his model in various ways (2 to 4). Taylor's paper presents the simplest possible two-dimensional (2D) model of sperm locomotion although it ignores many important aspects of actual sperm.

Mammalian sperm are made up of three main parts: the head (which holds the DNA cargo), the midpiece (which provides energy in the form of adenosine-triphosphate) and the tail or flagellum

[†](njb@math.ubc.ca)

(5). The human sperm flagellum is a long, slim structure (typically 50–60 μm long and around 200 nm in diameter). The core of the flagellum consists of an array of parallel microtubules along with energy-consuming dyneins (molecular motors) that push the microtubules past each other. By periodically activating dyneins on opposite sides of the flagellum, the sperm generates local bending moments. These forces work against the external fluid to produce the shape of the flagellum. Indeed, the wave-form of a swimming sperm has been observed to vary according to the medium in which it is swimming (6, 7). In the case of mammalian sperm, this has biological importance since they swim in a variety of media during their journey to the egg. The viscoelastic properties of cervical mucus have been studied in some detail, and the rheological parameters are found to vary with the menstrual cycle (8, 9). It is therefore of interest to revisit Taylor’s calculations but in the context of actively working organisms within a complex fluid.

In the current article, we follow along the lines of Taylor’s original article in exploring aspects of swimming microorganisms from an analytical perspective. Our interest focuses on the variant of the problem in which the swimmer moves beside a wall and inside a fluid that is not necessarily Newtonian, both of which have a number of important applications to biological locomotion (2, 10 to 14). For example, the motion of sperm close to solid boundaries is of biological interest since mammalian sperm commonly travel through tube-like organs (such as the oviducts). Furthermore, the dynamics of a non-Newtonian fluid layer sandwiched between flexible walls is also relevant to some other biological problems, such as cartilage and cell mechanics (for example (15, 16)) and the adhesion of insects and other organisms to walls (for example (17, 18)), in addition to the more traditional applications in engineering lubrication (19).

To make analytical inroads into the problem, our analysis exploits Reynolds lubrication theory, which applies when the fluid layer under consideration is relatively thin and the swimmer moves sufficiently slowly to use the Stokes approximation. This route was previously taken by Katz (2), Chan *et al.* (20) and Wilkening and Hosoi (21) to generalise Taylor’s work. Chan *et al.* also allowed the fluid to be viscoplastic in order to expand on Denny’s work on snail locomotion (10, 11). Other earlier works that treat non-Newtonian (and specifically viscoelastic) fluids mostly follow Taylor’s original direction in exploiting the low-amplitude limit for a swimmer immersed in an infinite expanse of fluid (14, 22 to 26). In our work, the lubrication approximation simplifies many of the details of the governing equations and facilitates a discussion of much larger amplitude motions. Moreover, we are also able to incorporate additional dynamics of the swimmer itself: much like existing models of the dynamics of animals swimming at much higher Reynolds numbers (3), we explicitly include the force balance on the swimmer, assuming that it behaves as a flexible elastic sheet (rather than fixing the shape of the swimming motion, the route taken in many of the earlier articles on swimming microorganisms). We are thereby able to offer a variety of analytical results to complement recent, fully computational efforts (12, 27, 28).

The key physical questions that we address are as follows. For a flexible swimmer in a viscous fluid, we explore how the wave shape and speed are determined by a combination of the fluid dynamics in the gap separating the swimmer from the wall and the solid mechanics of the swimmer itself, assuming the latter to be driven by an imposed, prescribed force (cf. (23, 29, 30)). With a complex fluid, we investigate how the swimmer profile is affected by non-Newtonian effects, focusing specifically on two hallmarks of viscoplastic fluids: shear-rate-dependent viscosity (shear thinning or thickening) and a yield stress, both of which are commonly encountered properties of polymeric gels and suspensions (31). A variable viscosity impacts swimmers as the rate of locomotion changes the effective fluid resistance. Though not previously considered in the swimming context, yield stresses endow the swimmer’s environment with an intrinsic strength that must be exceeded

in order for the swimmer to propel itself forward. Part of our goal is to characterise that threshold for motion. However, a yield stress also enriches the fluid dynamics even once the swimmer is moving, with rigid plugs and nearly rigid zones (‘pseudo-plugs’) disfiguring flow patterns (for example, (28)), and we expose how this modifies Katz’s swimming problem. Yield stresses have not often been measured for biological fluids like mucus (except for snail slime (11, 32)), with such media more usually characterised as viscoelastic. Mud and sediment, though, are typically viscoplastic, suggesting applications to the locomotion of marine organisms.

In section 2, we outline the mathematical formulation of the problem. Section 3 deals with viscous fluids, exploring the effects of swimmer stiffness. Section 4 considers the corresponding non-Newtonian problem. Section 5 offers some consideration of the effect of the head and tail of the swimmer by abandoning the periodic boundary conditions used earlier and imposing conditions suitable for a finite swimmer.

2. Mathematical formulation

2.1 Dimensional equations

Consider a 2D layer of an incompressible fluid of density ρ sandwiched between a plane wall and a flexible surface that ‘swims’ slowly forward by exerting a transverse force to create travelling, undular motions along its length (Fig. 1). The fluid is described by its pressure $\hat{p}(\hat{x}, \hat{y}, \hat{t})$ and velocity field $(\hat{u}(\hat{x}, \hat{y}, \hat{t}), \hat{v}(\hat{x}, \hat{y}, \hat{t}))$, referring to the Cartesian coordinate system shown in Fig. 1. The swimmer has a speed U and our coordinate system is located in the translating frame of the swimmer, so that the wall translates to the left and the flexible upper surface moves purely vertically in the figure. For most of our study, the configuration is taken to be periodic in x , so we avoid discussion of the swimmer’s head and tail. However, in section 5, we will discuss finite-length swimmers and impose boundary conditions in x .

We assume that the layer is thin, and the fluid’s material properties are such that the resistance to sheared flow is dominated by the shear stress $\hat{\tau}(\hat{x}, \hat{y}, \hat{t})$ (as it would be for a large class of non-Newtonian fluid models, see also Appendix A). In this situation, we may exploit Reynolds’ lubrication approximation to simplify the governing equations for the fluid to

$$\hat{u}_{\hat{x}} + \hat{v}_{\hat{y}} = 0, \quad \hat{p}_{\hat{x}} = \hat{\tau}_{\hat{y}}, \quad \hat{p}_{\hat{y}} = 0, \tag{2.1}$$

representing conservation of mass and momentum (in the absence of fluid inertia). Subscripts represent partial derivatives. As indicated by Fig. 1, the velocity boundary conditions are

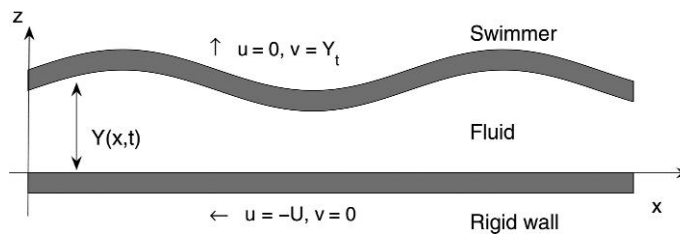


Fig. 1 A sketch showing the geometry of the problem in the (horizontally) translating frame of the swimmer

$$\hat{u}(\hat{x}, 0, \hat{t}) = -\hat{U}, \quad \hat{v}(\hat{x}, 0, \hat{t}) = 0 \quad \text{and} \quad \hat{u}(\hat{x}, \hat{Y}, \hat{t}) = 0, \quad \hat{v}(\hat{x}, \hat{Y}, \hat{t}) = \hat{Y}, \quad (2.2)$$

where $\hat{y} = \hat{Y}(\hat{x}, \hat{t})$ denotes the position of the swimming surface.

We complement the system in (2.1)–(2.2) with a constitutive law for the potentially non-Newtonian fluid, which we assume to take the functional form

$$\hat{\tau} = T(\dot{\gamma}) \quad \text{or} \quad \dot{\gamma} = \Gamma(\hat{\tau}), \quad (2.3)$$

where the deformation rate $\dot{\gamma}$ is given predominantly by the shear rate $\hat{u}_{\hat{y}}$ in the slender geometry of the fluid. By way of examples, we consider two prototypical functions for $T(\dot{\gamma})$. The first is a simple kind of generalised Newtonian fluid that incorporates a rate-dependent viscosity:

$$T(\hat{u}_{\hat{y}}) = \left(\frac{1 + \hat{a}\hat{u}_{\hat{y}}^2}{1 + \hat{\beta}\hat{u}_{\hat{y}}^2} \right) \eta \hat{u}_{\hat{y}}, \quad (2.4)$$

where η represents a reference viscosity and \hat{a} and $\hat{\beta}$ denote dimensional rheological constants controlling the degree of shear thinning or thickening. As shown in Appendix A, this model also corresponds to a wide class of viscoelastic fluid models for our slender fluid geometry (which become quasi-steady under certain assumptions concerning fluid relaxation times; see Appendix A). The second example is the Bingham fluid (31), for which

$$T(\hat{u}_{\hat{y}}) = \left(\eta + \frac{\tau_Y}{|\hat{u}_{\hat{y}}|} \right) \hat{u}_{\hat{y}} \quad \text{if } |\hat{\tau}| > \tau_Y, \quad (2.5)$$

which corresponds to the yielded state, and $\hat{u}_{\hat{y}} = 0$ otherwise (when the fluid is rigid); here, τ_Y is the yield stress.

Finally, we assume that the swimmer is also thin and can be modelled as an elastic beam, a membrane or a (Winkler) foundation. We consider these three models because they offer the simplest mathematical description of slender elastic sheets in which the dominant restoring force is from bending stiffness, membrane tension or spring-like attachment to a rigid backing, respectively. All three models may have biological application, with the foundation providing a possible model for a muscular layer attached to a more rigid support structure as in a mollusc's foot.

As a first approximation, we will ignore fluid resistance from above as may be true if the fluid layer above the swimmer is much thicker than the underlying lubrication layer. Force balance in the direction normal to the wall then demands that

$$\hat{p}(\hat{x}, \hat{Y}, \hat{t}) = \hat{D} \left(-\frac{\partial^2}{\partial \hat{x}^2} \right)^n \hat{Y} + \hat{f}(\hat{x}, \hat{t}), \quad (2.6)$$

where the constant \hat{D} measures the stiffness of the swimmer and the power n allows us to switch from the beam ($n = 2$) to the membrane ($n = 1$) or foundation ($n = 0$). The function $\hat{f}(\hat{x}, \hat{t})$ represents a transverse force exerted on the swimmer that generates its undular motions. We take

$$\hat{f}(\hat{x}, \hat{t}) = \hat{A} \sin K(\hat{x} + c\hat{t}), \quad (2.7)$$

where the wave speed c , amplitude \hat{A} and wavelength $2\pi/K$ are prescribed.

The force balance parallel to the wall provides an equation of motion for the swimmer that determines its speed:

$$\hat{M} \frac{d\hat{U}}{d\hat{t}} = -W \int_0^{2\pi/k} [\hat{\tau}(\hat{x}, \hat{Y}, \hat{t}) + \hat{Y}_{\hat{x}}(\hat{x}, \hat{t}) \hat{p}(\hat{x}, \hat{Y}, \hat{t})] d\hat{x}, \quad (2.8)$$

where \hat{M} denotes the (reduced) mass of the swimmer over the period of the imposed force and W is its effect width. Note that the inclusion of the swimmer's longitudinal inertia is justified when that object is massive in comparison to the fluid layer (allowing the Stokes approximation for the fluid) yet still relatively thin (justifying the neglect of the transverse inertia in (2.6)).¹ For most of the biological examples that motivate this study, inertia could be neglected but for our main focus, steady swimming, the inertial term vanishes in any case.

2.2 Dimensionless system

We remove the dimensions from the equations by defining dimensionless variables that are free of the hat decoration:

$$x = K\hat{x}, \quad y = \frac{\hat{y}}{H}, \quad Y = \frac{\hat{Y}}{H}, \quad t = kc\hat{t}, \quad U = \frac{\hat{U}}{c}, \quad p = \frac{H\hat{p}}{\eta c} \quad \text{and} \quad \tau = \frac{\hat{\tau}}{k\eta c}, \quad (2.9)$$

where H is the mean thickness of the fluid layer. With this change of variables, the fluid equations (2.1) and boundary conditions (2.2) are unchanged but for the omission of the hats. The constitutive law becomes a dimensionless functional relation $\tau = T(u_y)$. For the two illustrative models,

$$T(u_y) = \frac{1 + \alpha u_y^2}{1 + \beta u_y^2} u_y \quad (2.10)$$

or

$$T(u_y) = u_y + B \text{sgn}(u_y) \quad \text{if } |\tau| > B \quad (\text{and } u_y = 0 \text{ otherwise}), \quad (2.11)$$

which uncovers the dimensionless parameters α and β , gauging the degree of shear thinning or thickening, and the Bingham number B that measures the importance of the yield stress. These parameters are defined in Table 1.

With these relations in hand, we observe that $p = p(x, t)$. Integrals of the other two fluid equations together with the constitutive law then imply that the surface shear rates $\dot{\gamma}_0 = u_y(x, 0, t)$ and $\dot{\gamma}_1 = u_y(x, Y, t)$ and shear stresses $\tau_0 \equiv \tau(x, 0, t) = T(\dot{\gamma}_0)$ and $\tau_1 \equiv \tau_1(x, t) = T(\dot{\gamma}_1)$ must satisfy the differential-algebraic system

$$Y_t + q_x = 0, \quad \tau_0 = \tau_1 - Y p_x, \quad U = \int_0^Y u_y dy = \frac{I_0}{p_x}, \quad (2.12)$$

$$q(x, t) = \int_0^Y u dy = \int_0^Y (Y - y) u_y dy - UY = \frac{U \tau_1}{p_x} - \frac{I_1}{p_x^2} - UY \quad (2.13)$$

¹ More specifically, scaling analysis indicates that fluid inertia can be discarded provided $\rho c H / \eta \ll 1$, where H is the mean gap thickness. On the other hand, the ratio of the inertial term on the left of (2.8) to the forces on the right is of order $\hat{M} c K / \eta W$ and is therefore bigger than $\rho c H / \eta$ by a factor of $\hat{M} K / \rho H W$.

Table 1 Table of key dimensionless groupings

Symbol	Definition	
A	$\frac{H\hat{A}}{\eta c}$	Dimensionless forcing amplitude
M	$\frac{kc\hat{M}}{2\pi\eta\bar{W}}$	Dimensionless sheet mass
D	$\frac{H^2k^{2n}\hat{D}}{\eta c}$	Dimensionless sheet stiffness
α, β	$\frac{c^2\hat{\alpha}}{H^2}, \frac{c^2\hat{\beta}}{H^2}$	Rescaled rheological parameters
B	$\frac{H\tau_Y}{\eta c}$	Bingham number

and

$$I_0 = \int_{\dot{\gamma}_0}^{\dot{\gamma}_1} T'(\dot{\gamma})\dot{\gamma} d\dot{\gamma}, \quad I_1 = \int_{\dot{\gamma}_0}^{\dot{\gamma}_1} T(\dot{\gamma})T'(\dot{\gamma})\dot{\gamma} d\dot{\gamma}. \quad (2.14)$$

The dynamics of the swimmer are governed by

$$p(x, Y, t) = D \left(-\frac{\partial^2}{\partial x^2} \right)^n Y + A \sin(x + t) \quad (2.15)$$

and

$$M\dot{U} = - \int_0^{2\pi} [\tau_1(x, t) - Y(x, t)p_x(x, t)] \frac{dx}{2\pi} = - \int_0^{2\pi} \tau_0(x, t) \frac{dx}{2\pi}, \quad (2.16)$$

where the dimensionless amplitude, mass and stiffness parameters (A , M and D , respectively) are defined in Table 1.

Equations (2.12)–(2.16) constitute the key equations of the problem. The main dependent variables are $Y(x, t)$ and $U(t)$, satisfying the integral conservation of mass equation $Y_t + q_x = 0$ and the longitudinal equation of motion (2.16). From these variables, using (2.15) and the algebraic equations in (2.12), we compute p_x and then τ_0 and τ_1 or $\dot{\gamma}_0$ and $\dot{\gamma}_1$. The flux q and integrated basal shear stress $\int \tau_0 dx$ can then be computed via (2.13) to complete the evolution equations.

3. Periodic viscous swimming

3.1 The initial-value problem

For Newtonian fluids, (2.12)–(2.16) simplify to

$$Y_t = \left(\frac{1}{2}UY + \frac{1}{12}Y^3 p_x \right)_x, \quad M\dot{U} = - \int_0^{2\pi} \left(\frac{U}{Y} - \frac{1}{2}Y p_x \right) \frac{dx}{2\pi} \quad (3.1)$$

and

$$p = A \sin(x + t) + D(-\partial_x^2)^n Y. \quad (3.2)$$

We solve this (periodic in x) system numerically as an initial-value problem, starting from a flat motionless swimmer $Y(x, 0) = 1$ and $U(0) = 0$. We compute spatial derivatives on a uniform grid of 10^3 points using either centred finite differences or the fast Fourier transform and advance in time using a standard adaptive integrator. An illustrative example is shown in Fig. 2. After a transient initial adjustment, the swimmer settles into a steady state with constant speed.

In the limit of low amplitude, the system (3.1)–(3.2) can be solved analytically by a regular perturbation expansion. For a beam ($n = 2$), we find the profile converges to

$$Y \sim 1 + \frac{A}{144 + D^2} [12 \cos(x + t) - D \sin(x + t)]. \quad (3.3)$$

Inserting this profile into the second relation in (3.1) implies

$$U \sim \frac{3A^2(1 - e^{-t/M})}{(144 + D^2)} \quad (3.4)$$

(the complete solution to the initial-value problem adds an additional decaying oscillation in U). These predictions are also included in Fig. 2, where they adequately match the numerical results, despite the relatively large value of $A = 1$ used in the computation.

Note that the evolution equation in (3.1) becomes hyperbolic in the limit that $D \rightarrow 0$ since p is then prescribed: $p \rightarrow A \sin(x + t)$. Such a swimmer is infinitely flexible and the imposed force must be balanced purely by the resistive fluid pressure. Although the characteristic equations for this system cannot be solved analytically (one learns that the quantity $[6UY + AY^3 \cos(x + t)]/12$ is conserved along the characteristic curves, but the unknown time dependence of U prevents one integrating analytically for those curves), the mathematical structure suggests that it may be possible for the swimmer to generate shock-like profiles at higher forcing amplitudes. Indeed, we see shortly that this is inescapable once A exceeds a critical threshold.

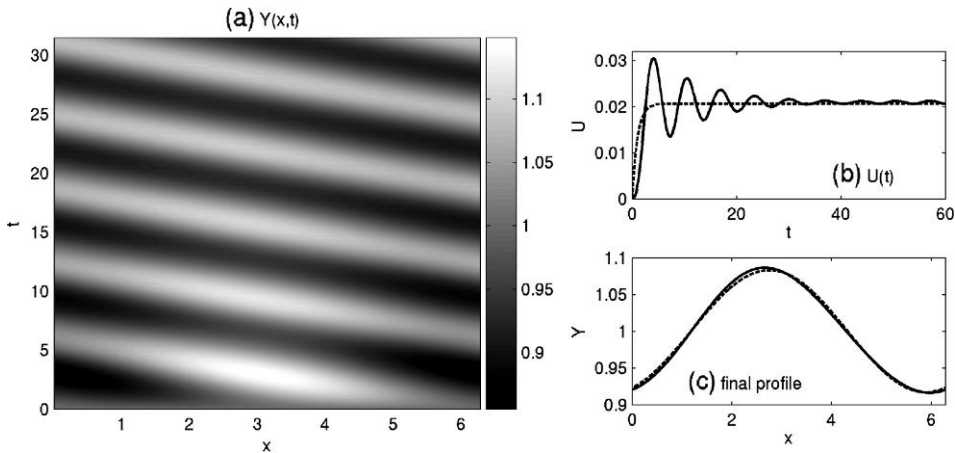


Fig. 2 Solution of the viscous initial-value problem with $A = D = M = 1$ and $n = 2$. Panel (a) shows initial evolution of the swimmer surface position, $Y(x, t)$, as a density on the (x, t) -plane. Panel (b) shows the swimmer speed together with the low-amplitude approximation (3.4). Panel (c) shows the final profile and the prediction (3.3)

3.2 Steady swimming

The steady swimming state can be computed directly from the nonlinear eigenvalue problem

$$Q = \left(1 - \frac{1}{2}U\right)Y - \frac{1}{12}Y^3 p_\zeta, \quad D(-\partial_\zeta^2)^n Y_\zeta = p_\zeta - A \cos \zeta, \quad (3.5)$$

where $\zeta = x + t$, and the eigenvalues U and Q must be chosen to satisfy the integral constraints

$$\int_0^{2\pi} Y \frac{d\zeta}{2\pi} = 1, \quad \int_0^{2\pi} \left(\frac{U}{Y} - \frac{1}{2}Y p_\zeta\right) \frac{d\zeta}{2\pi} = 0, \quad (3.6)$$

the first of which corresponds to conservation of total fluid underneath the swimmer (the spatial integral of $Y_t + q_x = 0$, given the periodic boundary conditions and the choice of the mean gap thickness H to scale lengths).

We first consider the case of an infinitely flexible surface (that is, $D = 0$). In this limit, the differential character of the problem is avoided and the swimmer profile follows from the implicit algebraic relation

$$\cos \zeta = \frac{12}{A} \left[\frac{(2-U)}{2Y^2} - \frac{Q}{Y^3} \right]. \quad (3.7)$$

Unfortunately, U and Q remain unknown until one imposes the integral constraints in (3.6), and numerical resolution of the eigenvalue problem is still needed. Examples of computed steady swimmer shapes are shown in Fig. 3. The swimmer speed increases with forcing amplitude slightly faster than expected from (3.4). More importantly, the solution branch also appears to terminate at a particular value of $A \approx 1.904$ (see Fig. 4). As we approach that termination point, the solution develops a sharp corner at its maximum and, beyond, the solution no longer remains continuous. We interpret this breakdown as the appearance of a shock in the hyperbolic, $D = 0$, problem.

To regularise the system and smooth the discontinuous solutions at higher amplitude, we include a finite stiffness. Regularised solutions at $A = 2.5$ for a beam with varying stiffness are shown in Fig. 5 and for different elastic swimmers (that is, n) in Fig. 6. These solutions contain ‘stiffened boundary layers’ over which the solution remains smooth if sharply varying. (In Fig. 6, the values of D for the different cases of n are chosen to give similar shock thicknesses.)

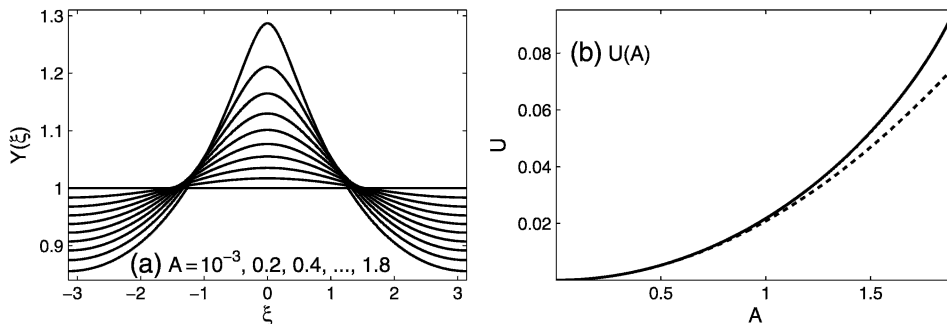


Fig. 3 (a) Infinitely flexible ($D = 0$), steady swimmer profiles, $Y(\zeta)$, for varying forcing amplitude ($A = 10^{-3}, 0.2, 0.4, \dots, 1.8$). (b) Swimming speeds versus forcing amplitude; the low-amplitude prediction (3.4) is shown by the dashed line

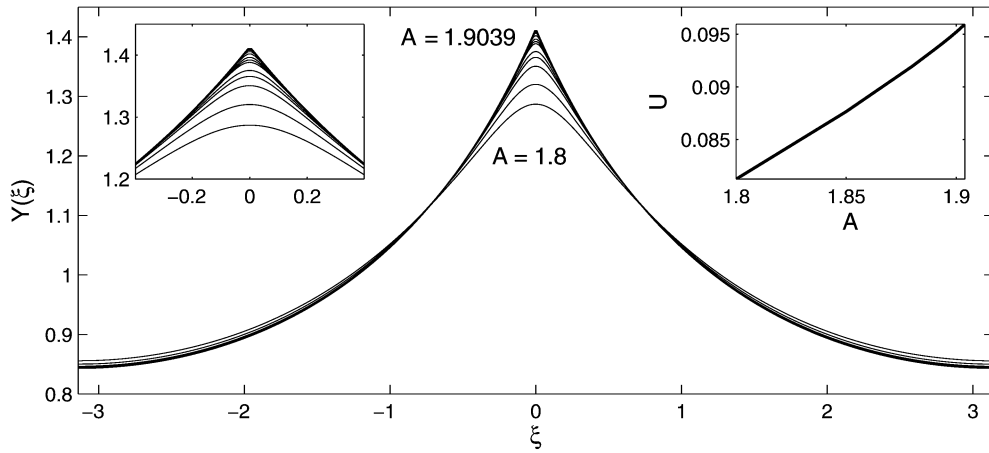


Fig. 4 Infinitely flexible ($D = 0$), steady swimmer profiles, $Y(\xi)$, for varying forcing amplitude ($A = 1.8, 1.85, 1.88, 1.89, 1.895, 1.9, 1.901, 1.902, 1.903, 1.9035, 1.9037, 1.9038$ and 1.9039). The insets show a magnification near the peak in $Y(\xi)$ and the swimming speed

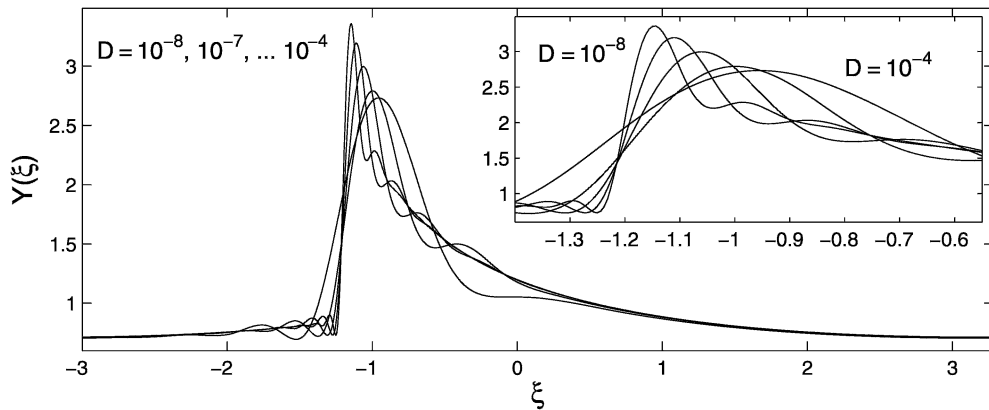


Fig. 5 Steady swimmer profiles for $A = 2.5, n = 2$ and varying values of stiffness D

Another perspective on the emergence of discontinuous profiles for $D = 0$ is shown in Fig. 7, which shows the multi-valued solutions of the implicit equation for Y in (3.7), for four different values of A . To compute these solutions, we use the speed and flux calculated for the regularised problem, assuming a beam with a finite stiffness of $D = 10^{-7}$; that numerical solution is also included in the figure. At low amplitude, it is possible to construct a smooth profile with $D = 0$ using the lowest solution branch shown in the figure (panels (a) and (b)). At higher amplitude, however, the topology changes and that branch connects to the upper solution; smooth profiles cannot then be built without adding a stiffened boundary layer (panels (c) and (d)). Importantly, a passage through the maximum of the right-hand side of (3.7) (given by $2(2-U)^3/9Q^2A$ and arising for $Y = 3Q/(2-U)$) is necessary at $\xi = 0$, implying $Q^2 = 2(2-U)^3/9A$. From the figure, it

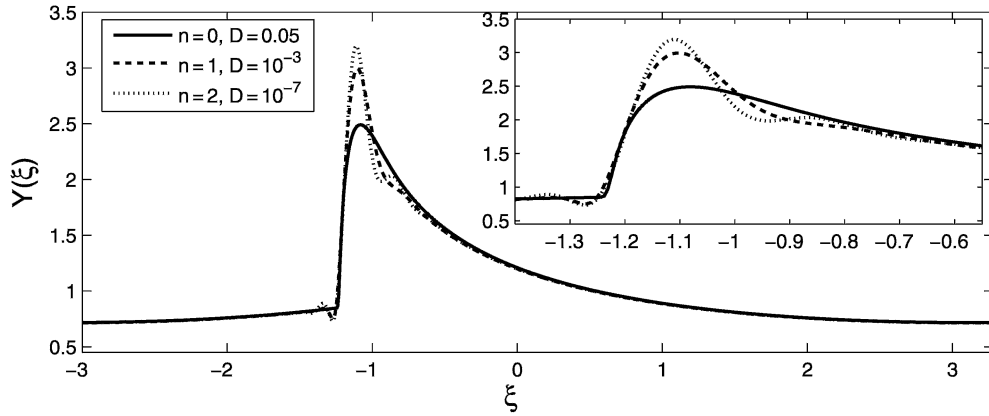


Fig. 6 Steady swimmer profiles for $A = 2.5$ and the three pairs of values of (n, D) indicated

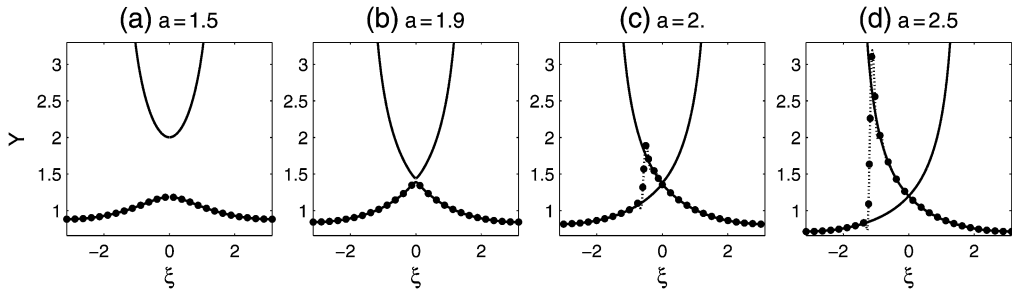


Fig. 7 The multi-valued solutions of (3.7) for $A = 1.5, 1.9, 2$ and 2.5 . These are computed using the values of U and Q determined for regularised solutions with $(n, D) = (2, 10^{-7})$, which are shown by the dotted lines

is apparent how one can compute discontinuous solutions with $D = 0$ by inserting a shock into profiles extracted from (3.7) and choosing its location and U to ensure that the integral constraints (3.6) are satisfied.

To continue the solutions to still higher A , we consider a swimming beam ($n = 2$); sample high-amplitude solutions are shown in Fig. 8. As the amplitude is raised, an increasingly wide section of the swimmer flattens out close to the wall. Simultaneously, the swimming speed reaches a maximum and then declines because of the heightened viscous resistance. Consequently, there is an optimal swimming speed, which is about $A \approx 5.1$ in the figure. In other words, beyond some limit, increasing the amount of force does not speed up the swimmer but merely allows it to press closer to the wall.

3.3 Very high-amplitude swimmers

The largest amplitude solutions shown in Fig. 8 develop a pulse-like structure that emerges from a low- Y plateau; two further examples at yet higher amplitude are displayed in Fig. 9. Note that the narrow fluid gaps trap a constant-pressure bubble beneath the localised pulse (see Fig. 9).

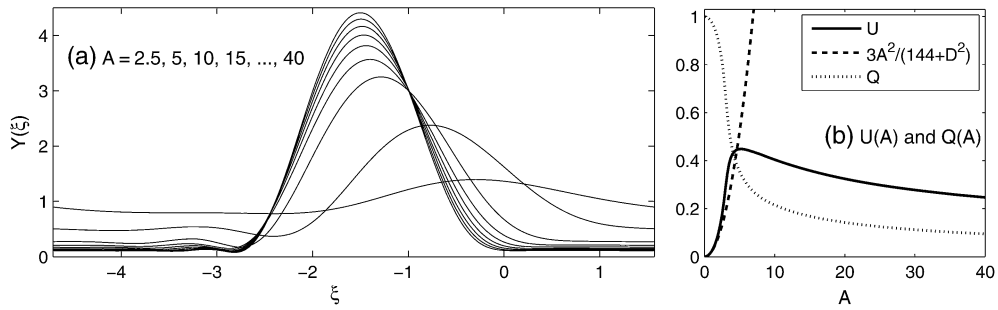


Fig. 8 Steady swimmer profiles for $A = 2.5, 5, 10, 15, \dots, 40$ and $(n, D) = (2, 0.1)$. The second panel shows the swimming speed U and effective flux Q against A

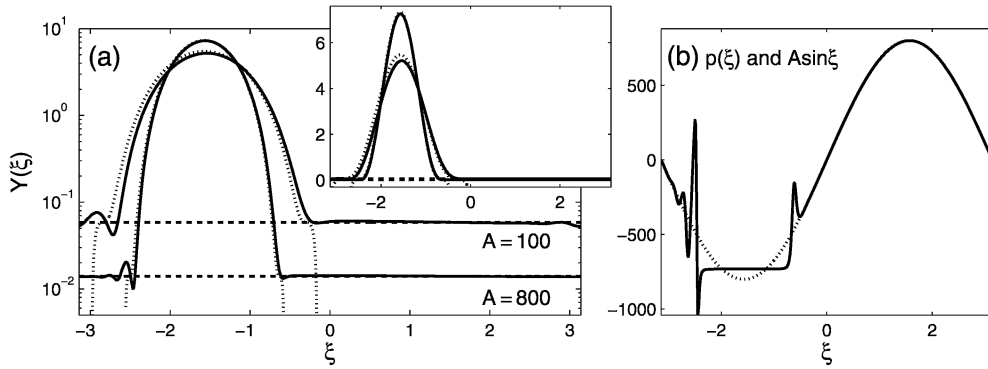


Fig. 9 (a) Steady swimmer profiles for $A = 100$ and 800 , with $(n, D) = (2, 0.1)$. The dotted line shows the asymptotic approximation in (3.10), and the dashed line is the level $Y = Q/(1 - U/2)$. (The $A = 800$ solution is the highest.) (b) The pressure field of the profile with $A = 800$ together with $A \sin \xi$

We rationalise the pulse-like structure of the solutions as follows. First, the effective flux Q and swimming speed U both become small in the large-amplitude limit (see Fig. 10). Consequently, from (3.5), the roughly constant, low- Y level to which the solutions converge is given by

$$Y \sim Y_* = \frac{2Q}{2 - U} \approx Q \quad \text{and} \quad p_\xi \sim A \cos \xi, \quad (3.8)$$

in agreement with the solutions of Fig. 9.

Second, $Y(\xi)$ is of order one within the main peak of the pulse-like solution, which is again consistent with (3.5) only if

$$p_\xi \sim \frac{12}{Y^2} \ll A |\cos \xi| \longrightarrow DY_{\xi\xi\xi\xi\xi} \sim -A \cos \xi. \quad (3.9)$$

Bearing in mind the symmetry of the peak about $\xi = -\frac{1}{2}\pi$ and the requirement that the solution match to the constant level in (3.8) at the edges of the peak $\xi \sim -\pi/2 \pm \xi$ (demanding

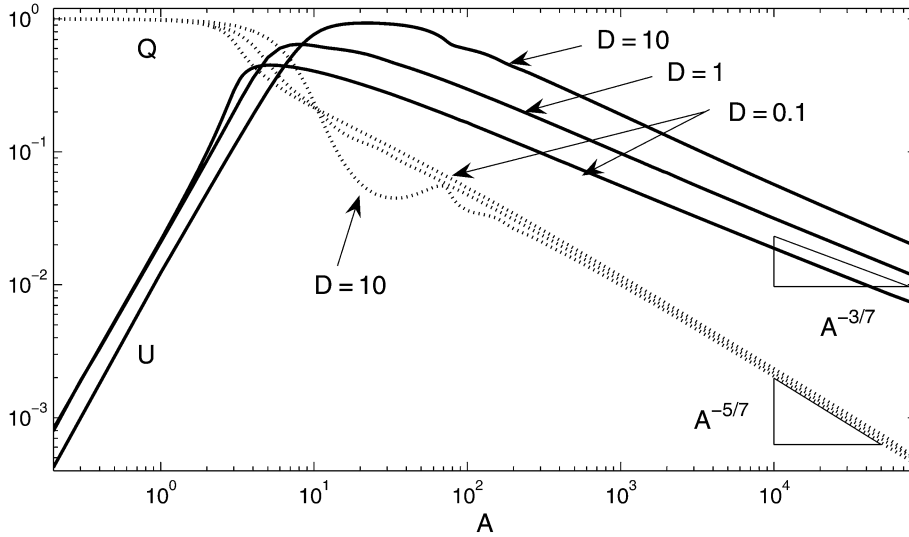


Fig. 10 Swimming speed U and flux Q versus forcing amplitude A for three values of D (0.1, 1 and 10), $n = 2$. The expected large-amplitude scalings $Q \sim A^{-5/7}$ and $U \sim A^{-3/7}$ are also indicated

$(Y, Y_\zeta, Y_{\zeta\zeta}) \rightarrow (Y_*, 0, 0)$ as $\zeta \rightarrow \pm\zeta$, the peak profile must therefore be given by

$$Y \sim Y_* + \frac{1}{24} p_0 \left[\left(\zeta + \frac{1}{2}\pi \right)^2 - \zeta^2 \right]^2 - \frac{A}{D} (\sin \zeta + \cos \zeta) + \frac{A \sin \zeta}{2D\zeta} \left[\left(\zeta + \frac{1}{2}\pi \right)^2 - \zeta^2 \right], \quad (3.10)$$

where

$$p_0 = \frac{3A}{D\zeta^3} (\zeta \cos \zeta - \sin \zeta) \quad (3.11)$$

is the pressure level in the trapped bubble. The edges of the peak are then determined by the leading-order part of the first constraint in (3.6):

$$2\pi \sim \int_{-\zeta}^{\zeta} Y d\zeta \sim \frac{2A}{D} \left[\left(1 - \frac{2\zeta^2}{5} \right) \sin \zeta - \zeta \left(1 - \frac{\zeta^2}{15} \right) \cos \zeta \right] \quad (3.12)$$

(ignoring the background level $Y_* \equiv Q/(1 - U/2)$, which makes a negligible contribution in comparison to the 2π). These relations indicate that $\zeta \sim (1575\pi D/A)^{1/7}$ for $A/D \gg 1$, which in turn implies that the peak height is $(155\pi)^{6/7} (A/D)^{1/7} / 720$. The relatively small powers of A in these expressions illustrate the slow rate of convergence to the asymptotic, large-amplitude limit.

Note that the solution in (3.10) corresponds to a curious kind of indentation problem: it describes the deflection of a beam that is clamped at $\zeta = -\pi/2 \pm \zeta$ and subject to a transverse force $p_0 - A \sin \zeta$. Both the edge position ζ and the pressure level p_0 are unknown, however, and chosen to select the correct area of the bubble and to ensure that no forces act at the edges ($Y_{\zeta\zeta} = 0$ at $\zeta = -\pi/2 \pm \zeta$). The swimmer's fluid mechanics supplement this 'punch' problem by determining the flux Q : the jumps in pressure that effectively arise at the edges of the peak (see Fig. 9) reflect

bottlenecks in the flow that control the flux into and out of the peak region (as in some other elasto-hydrodynamics lubrication problems, see (33)).

Unfortunately, the analysis to determine Q is significantly complicated by the structure of the finely scaled boundary layers surrounding the edges of the peak over which the pressure jump occurs. These layers are visible in Fig. 9 and are characterised by a combination of all three terms in the governing equation $DY_{\xi\xi\xi\xi} = p - A \sin \xi$ (cf. the structure evident in Fig. 9). The difficulty is that although we may extract the characteristic scales for the boundary layers' thickness $A^{-3/7}$ and the flux $Q \sim A^{-5/7}$, the solutions themselves follow from integrating a nonlinear, fifth-order differential equation ($v'''' = (v-1)/v^3$, with $v = Y/Y_*$, but expressed in terms of a boundary-layer coordinate) and then matching to the exterior solutions. We avoid those details here and satisfy ourselves that the predicted scaling of Q matches numerical computations (see Fig. 10). Moreover, the second constraint in (3.6) can be used to verify that $U \sim A^{-3/7}$ again in agreement with the computations.

4. Swimming in slime

4.1 Effects of shear thickening or thinning

We next display the results of allowing the fluid to be shear thinning or thickening according to the model (2.10). When the stress function $\tau = T(\dot{\gamma})$ is not linear, (2.12)–(2.14) must be formally inverted for $\dot{\gamma}_0$ and $\dot{\gamma}_1$, given Y and p_ξ , which we accomplish numerically with Newton iteration. The results are then fed into the time-independent versions of (2.16) and the first part of (2.12) to complete the equations to be integrated for the steady states. To streamline the discussion, we ignore the effect of varying the stiffness of the swimmer and set D to a relatively small value or zero although this does restrict the exploration to lower forcing amplitude.

Typical results are shown in Fig. 11. Increasing α at fixed β (the first panel of the figure) corresponds to a shear thickening fluid; increasing β at fixed α (second panel) makes the fluid shear

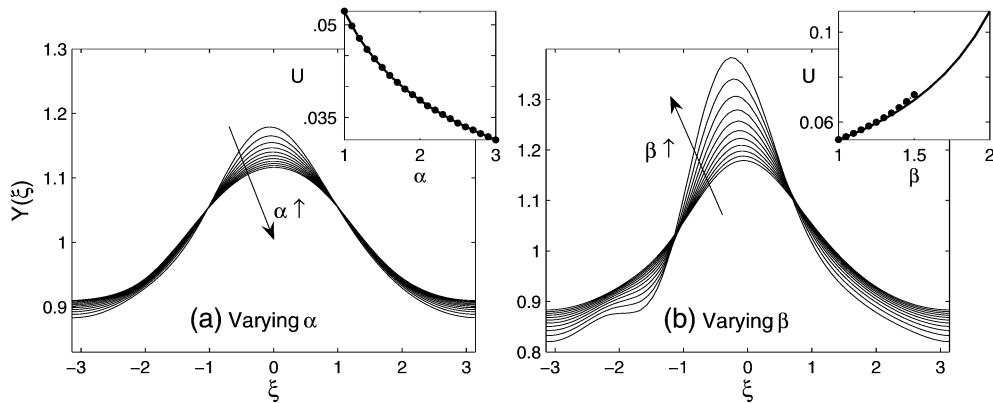


Fig. 11 Swimmer shapes for $A = 1.5$, $D = 0.01$, $n = 2$ and various values of α and β in the model (2.10). Panel (a) shows $\beta = 1$ and varying α (from 1 to 3, in steps of 0.2); panel (b) shows $\alpha = 1$ and varying β (from 1 to 2, in steps of 0.1). The insets show the swimming speed, and the dots show the results for $D = 0$. Note that the shear thinning solutions for $D = 0$ cease to exist just beyond $\beta = 1.5$ (and the solutions with $D = 0.01$ become increasingly asymmetric under reflection about $\xi = 0$)

thinning. Perhaps unsurprisingly, the figure illustrates how shear thickening lowers the swimmer's deflection and speed, whereas shear thinning amplifies and accelerates the swimming motion as found previously by Lauga and Hosoi (34) in a model of gastropod locomotion. The main consequence on the swimmer's profile is that shear thickening promotes a more sinusoidal shape (the pattern of the imposed forcing), whereas shear thinning makes the swimmer take on a more sharply peaked profile. Nevertheless, the viscosity variations incurred for the two examples shown in Fig. 11 are not particularly large (being a factor of 3 or 1/2, respectively). However, it is also possible to argue that the viscosity variations modelled by (2.10) have limited effect on the large-amplitude solutions considered in section 3.3 (using a generalisation of the same analysis).

Note that the generalised Newtonian fluid model (2.4) corresponds to the limit of a viscoelastic fluid in which shear thinning or thickening is the only appreciable effect (see Appendix A). Had we chosen fluids with relatively long relaxation times, the asymptotic ordering that leads to the current model would have been violated and a different theory is called for that incorporates the effects of time-dependent elasticity but is much less analytically tractable.

4.2 Overcoming a yield stress

4.2.1 Flow patterns. When the fluid has a yield stress, the problem becomes complicated by the possibility that certain regions are not stressed sufficiently to flow. Indeed, at forcing amplitudes that are too low, one expects that the swimmer is unable to break the rigid fluid layer underneath it and cannot therefore swim. In this section, we consider the Bingham fluid model (3.4) and determine the forcing required for the swimmer to move together with the form of the motion once swimming is underway. For brevity, we again focus on low-amplitude, infinitely flexible ($D = 0$) swimmers.

For this specific model, the formulation in (2.12)–(2.16) is unnecessarily general, and the analysis is assisted by some key simplifications resulting from a deeper exploration of the flow field. In part, the insights follow from considering the Newtonian flow field, an example of which is shown in Fig. 12. In the thin-gap geometry, $u(x, y, t)$ is parabolic in y , with the extrema reflecting the vanishing of the leading-order stress. Thus, one anticipates that rigid plugs might form around those extrema when a yield stress is present. Denoting the borders of those regions, the 'yield surfaces', by $y = Y_{\pm}$, with $Y_+ > Y_-$, and given that any sheared flow must still be parabolic, the possible flow profiles for u are sketched in the lower row of panels of Fig. 12.

To compute steady swimmer solutions, we discretise in x and adopt trial values for the pressure gradient p_{ξ} and swimmer position and speed Y and U . Given those, one can compute the flux Q , surface shear stress τ_1 and yield surfaces Y_{\pm} explicitly for each of the different types of flow profile. A summary of the main details of this construction is presented in Appendix B. The computed positions of Y_{\pm} can then be used to self-consistently identify which type of flow field arises at a given location underneath the swimmer, and a complete flow field can then be pieced together. The dynamical relations in (2.12), (2.15) and (2.16) now furnish constraints that one can satisfy after implementing a standard Newton iteration scheme to correct the trial values of p_{ξ} , Y and U .

Sample numerical solutions for four values of B are shown in Fig. 13. Displayed are plots of $Y_{\pm}(\xi)$ (the 'plug' regions) along with a number of other useful characteristics. The yield surfaces illustrate how the various flow profiles become pieced together to provide the full flow field (proceeding from left, $\xi = -\pi$, to right, $\xi = \pi$, the pattern is $C \rightarrow D \rightarrow E \rightarrow A \rightarrow B \rightarrow C \rightarrow B \rightarrow A \rightarrow E \rightarrow D \rightarrow C$, using the classification scheme of Fig. 12 and Appendix B).

The specific choices of Bingham number shown in Fig. 13 begin from a case close to the Newtonian limit, where the plugs are very thin. The plugs widen as the Bingham number increases.

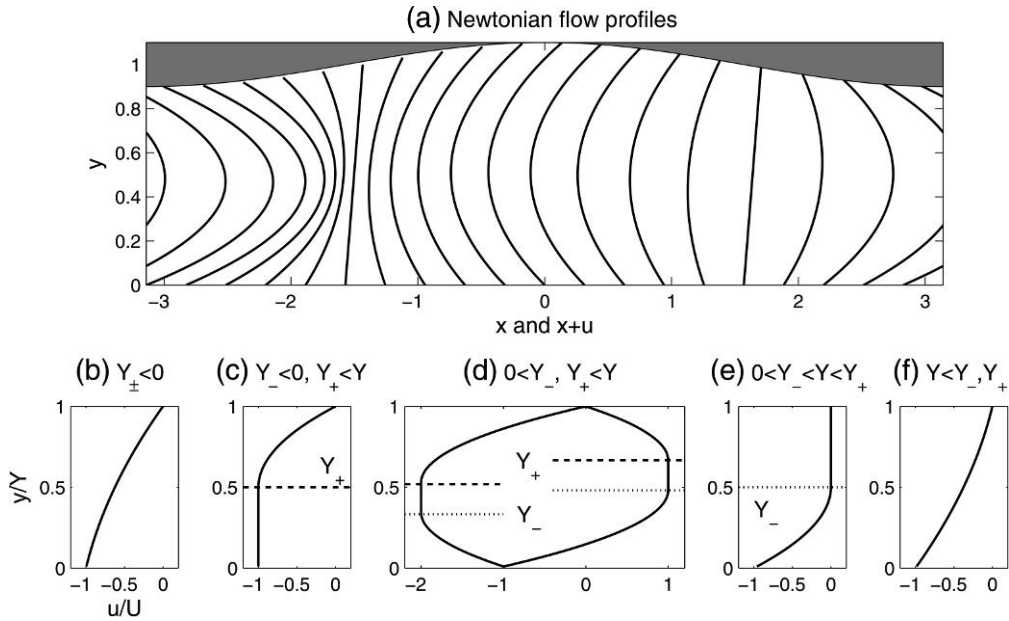


Fig. 12 Panel (a): Newtonian flow profiles for a low-amplitude swimmer. Panels (b)–(f) show the various possible flow profiles for the Bingham case, with the various positions for the two ‘yield surfaces’ (with two options in Panel (d)). These are, respectively, labelled cases **A**, **B**, **C**, **D** and **E** in Appendix B

In the final example, the swimmer is close to being brought to rest by the fluid yield stress, which is evidenced in the figure by the plugs nearly spanning the fluid layer close to $\zeta = \pm\pi/2$ and also by the plot of U against B . Note that where the plug regions adjoin either the swimmer or the underlying wall, the swimmer profile becomes relatively flat; simultaneously, one of the surface shear stresses remains close to the yield value. Also, the speed of the plug regions varies with ζ (see the final panel of the figure). Thus, those regions are not truly rigid and are examples of ‘pseudo-plugs’—regions held just above, but not below, the yield stress, which are commonly encountered in slender viscoplastic flows (35). Likewise, the Y_{\pm} do not represent true yield surfaces, merely the borders of the plug-like flow.

4.2.2 The stopping condition. To locate onset of motion more precisely, we make the following arguments. As illustrated by Fig. 13, complete vertical sections of the fluid become truly rigid and the swimmer is halted when the two yield surfaces touch the swimmer and wall simultaneously; that is, when $Y_+ \rightarrow Y$ and $Y_- \rightarrow 0$ at the same position. By examining the explicit form of the flow patterns to which this limiting behaviour corresponds (see Appendix B), we find

$$Y_+ = Y = \frac{2B}{|p\xi|} = Y_* \tag{4.1}$$

for the gap thickness where the plugs first fill the fluid layer. Once this occurs, a rigid static layer forms surrounding $\zeta = \pm\pi/2$ (see Fig. 13), within which the flux $\int u dy$ is zero in the frame of the swimmer. The flux in the frame of the waves is therefore $Q = Y_*$.

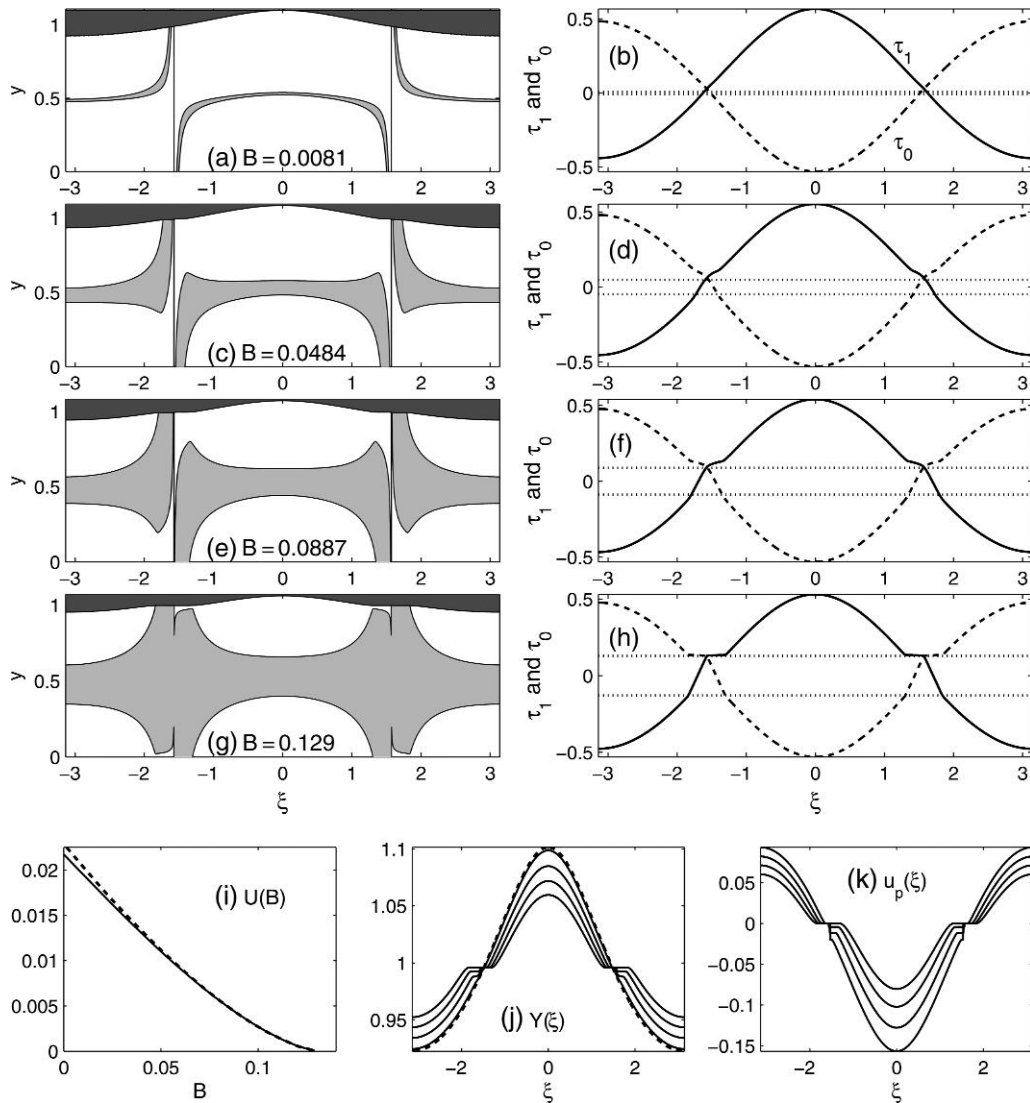


Fig. 13 Numerical solutions for the Bingham fluid model and a swimmer without stiffness ($D = 0$) and forcing amplitude $A = 1$. Four values of Bingham number, B , are displayed (as indicated). In Panels (a), (c), (e) and (f), the shaded regions show the swimmer (darker) and the ‘plug’ regions (lighter). Panels (b), (d), (f) and (h) show the surface stresses, τ_0 (dashed) and τ_1 (solid), along with $\pm B$ (dotted). The final row of panels show (i) the swimmer speed as a function of B (together with the fit, $U = 0.44(B - B_*)^{3/2}$ and $B_* = 0.1315$, shown by the dashed line), (j) a comparison of the swimmer shapes (the dashed curve shows the Newtonian swimmer profile) and (k) the plug speeds, $u_p(\xi)$ (which can be discontinuous near $\xi = \pm\pi/2$ when a plug region adjacent to one of the surfaces disappears)

Although the swimmer is now not moving, a yielded zone still persists containing a central pseudo-plug (the flow pattern of Fig. 12(d)). Within that region, $0 < Y_- < Y_+ < Y$, and the flow profile is (given that $p_\xi = \tau_y \equiv u_{yy}$ in the sheared parts of the flow)

$$u = \begin{cases} u_p + \frac{1}{2}p_\xi(Y_- - y)^2, & 0 < y < Y_-, \\ u_p, & Y_- < y < Y_+, \\ u_p + \frac{1}{2}p_\xi(y - Y_+)^2, & Y_+ < y < Y, \end{cases} \quad (4.2)$$

where the plug speed is

$$u_p = -\frac{1}{2}p_\xi(Y - Y_+)^2 = -\frac{1}{2}p_\xi Y_-^2, \quad (4.3)$$

which demands that $Y_- + Y_+ = Y$. The two surface shear stresses are $\tau_0 = -\frac{1}{2}Yp_\xi$ and $\tau_1 = \frac{1}{2}Yp_\xi$ and within the layer

$$\tau = \tau_0 + yp_\xi. \quad (4.4)$$

But $\tau = \pm B \text{sgn}(p_\xi)$ at $y = Y_\pm$, which further demands that

$$Y_+ - Y_- = \frac{2B}{|p_\xi|} \quad \text{or} \quad Y_\pm = \frac{1}{2}Y \pm \frac{B}{|p_\xi|}. \quad (4.5)$$

Given these results, we may compute the flux in the wave frame:

$$Q = Y - \frac{1}{3}p_\xi \left(Y + \frac{B}{|p_\xi|} \right) \left(\frac{1}{2}Y - \frac{B}{|p_\xi|} \right)^2. \quad (4.6)$$

Equation (4.6) determines $Y(\zeta)$ implicitly because $p_\xi = A \cos \zeta$ and $Q = Y_*$.

Finally, if $\zeta = \pi/2 \pm \zeta_*$, where $Y = Y_*$, the length of the truly rigid plugs is $2\zeta_*$. Hence, the total stress on those regions cannot exceed $2B\zeta_*$. In fact, the limiting stress distribution in Fig. 13 suggests that τ_0 is equal to $-B$ throughout the region $[\pi/2 - \zeta_*, \pi/2]$ and then increases up to $+B$ over $[\pi/2, \pi/2 + \zeta_*]$ throughout which $\tau_1 = -B$. This limiting behaviour is easily confirmed on examining the explicit formulae for the surface stresses as $U \rightarrow 0$ (see Appendix B). Thus,

$$\tau_0 = \begin{cases} -B, & \pi/2 - \zeta_* < \zeta < \pi/2, \\ -B - Y_*p_\xi, & \pi/2 < \zeta < \pi/2 + \zeta_*, \end{cases} \quad (4.7)$$

given (4.4). The constraints $\int Y d\zeta = 2\pi$ and $\int \tau_0 d\zeta = 0$ then demand that

$$\int_{-\pi/2+\zeta_*}^{\pi/2-\zeta_*} Y d\zeta + \int_{\pi/2+\zeta_*}^{3\pi/2-\zeta_*} Y d\zeta + 4\zeta_* Y_* = 2\pi \quad (4.8)$$

and

$$4\zeta_* B - 2AY_*(1 - \cos \zeta_*) = \int_{-\pi/2+\zeta_*}^{\pi/2-\zeta_*} Y p_\xi d\zeta + \int_{\pi/2+\zeta_*}^{3\pi/2-\zeta_*} Y p_\xi d\zeta \quad (4.9)$$

at the critical yield stress $B = B_*$, for which the swimmer is first brought to rest. Equations (4.6)–(4.9) determine Y , B_* and ζ_* ; numerical calculations showing these quantities as functions of forcing amplitude are shown in Fig. 14. The solutions extend well beyond the critical amplitude at which the Newtonian solution ceases to be smooth, owing to the reduction in the deflection of the

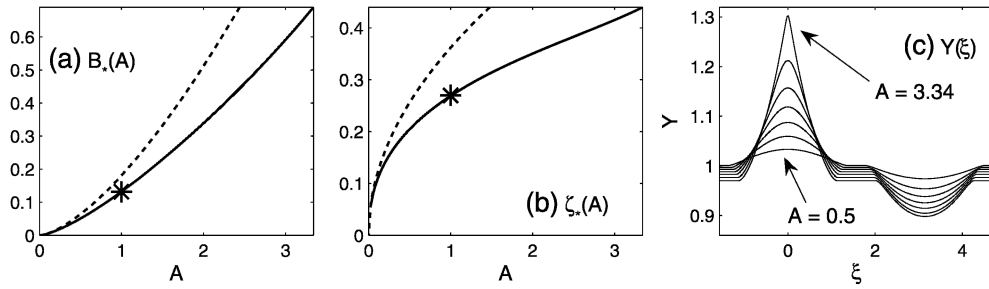


Fig. 14 Numerical solutions of the stopping condition problem showing (a) the critical yield stress, B_* , and (b) the half-width of the plug, ζ_* , as functions of A . The stars indicate the values expected from the computations shown in Fig. 13. The dashed lines show the low-amplitude limits $B_* \sim A^{3/2}\sqrt{\pi/96}$ and $\zeta_* \sim \sqrt{\pi}A/24$ (which follow from the shear stress constraint on noting the reductions $Y \sim 1 + p\xi/12$ and $Y_* = 2B/|p\xi| \rightarrow 1$). Panel (c) shows a selection of corresponding swimmer (for $A = 0.5, 1, 1.5, 2, 2.5, 3$ and 3.34)

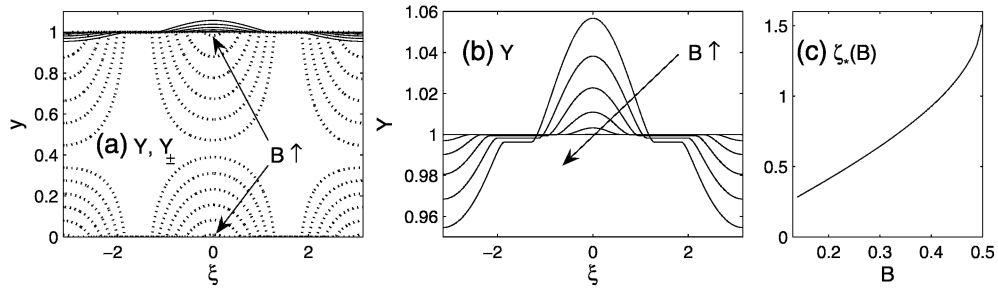


Fig. 15 Panels (a) and (b): Solutions for $Y(\xi)$ and $Y_{\pm}(\xi)$ below the stopping condition for $A = 1$ and six values of B (from 0.14 to 0.46 in steps of 0.8). Panel (c) shows the plug half-width, ζ_* , against B

swimmer due to the yield stress. However, at $A \approx 3.34$, the profile once again develops a corner (see Fig. 14), and a finite bending stiffness is needed to advance to higher amplitude.

Note that (4.2)–(4.6) remain valid even when $B > B_*$; that is, for yield stresses sufficient to hold the swimmer in place. In this situation, although the swimmer cannot make forward progress, sections surrounding the extrema of the imposed force are still able to move laterally according to the rhythm of the propagating wave. To compute the corresponding wave profiles, we use (4.2)–(4.6) and the mass conservation constraint in (4.8). However, the shear stress constraint (4.9) must be abandoned, leaving the plug half-thickness ζ_* as a function of B (the shear stress exerted by the stationary plugs need only exceed that from the yielded zones to ensure that the swimmer remain stationary). The widths of the sheared regions decrease with B , until motion ceases altogether for $\zeta_* \rightarrow \pi/2$ and $B \rightarrow A/2$, which is sufficient to ensure that the imposed forcing cannot break the yield stress anywhere underneath the swimmer.²

² When the swimmer is unable to deform, $Y = 1$ and $\tau_1 = \tau_0 + p\xi$. But both $|\tau_0|$ and $|\tau_1|$ cannot exceed B if the fluid is to remain unyielded, implying $2B \geq |\tau_1| + |\tau_0| \geq |\tau_1 - \tau_0| = A|\cos \xi|$, which is guaranteed for all ξ if $2B \geq A$.

5. A finite swimmer

5.1 Revisiting the initial-value problem

Thus far, we have explored the dynamics of infinite swimmers driven by spatially periodic disturbances travelling down their length. To offer some insight into the possible role of the head and tail of a finite swimmer, we now depart from this stance and impose alternative conditions at the ends. For simplicity and continuity, we take the ends to lie at $x = 0$ and $x = 2\pi$ and consider a propagating, sinusoidal-shaped forcing acting on a sheet with bending stiffness ($n = 2$). However, to accommodate the fact that the forcing needs no longer have the same period as that domain, we must now introduce another dimensionless parameter corresponding to the (not necessarily integral) wave number of the forcing k (demanding that we reinterpret the dimensional scale $2\pi/K$ as the swimmer's length). Thus, $f(x, t) = A \sin k(x + t)$.

The specific boundary conditions we impose are constant fluid pressure $p(0, t) = p(2\pi, t) = 0$ and a combination of either clamped or free conditions on the swimmer itself:

$$\begin{aligned} Y(0, t) = Y_x(0, t) = Y(2\pi, t) = Y_x(2\pi, t) &= 0 && \text{clamped-clamped,} \\ Y(0, t) = Y_x(0, t) = Y_{xx}(2\pi, t) = Y_{xxx}(2\pi, t) &= 0 && \text{clamped-free,} \\ Y_{xx}(0, t) = Y_{xxx}(0, t) = Y(2\pi, t) = Y_x(2\pi, t) &= 0 && \text{free-clamped,} \\ Y_{xx}(0, t) = Y_{xxx}(0, t) = Y_{xx}(2\pi, t) = Y_{xxx}(2\pi, t) &= 0 && \text{free-free.} \end{aligned} \quad (5.1)$$

Free-free is probably most relevant for a swimmer without a large head but we consider all four options in order to offer some insight into the range of possibilities without considering detailed physiology. Unfortunately, all such conditions prohibit us from shifting into the frame of the wave in order to find steadily propagating solutions; instead, we must resort to a solution of the initial-value problem to determine the swimming dynamics. That is, we return to (3.1)–(3.2) with $Y(x, 0) = 1$ and $U(0) = 0$ together with the new form for $f(x, t)$ and the boundary conditions.

A sample solution to the initial-value problem for a swimmer clamped at its head and tail is shown in Fig. 16. After a transient, the swimmer settles into a periodic state which is also displayed in the figure. For low forcing amplitude, the swimmer oscillates symmetrically about $Y = 1$; such states can be predicted largely analytically by examining the limit $A \ll 1$ as described momentarily (results for $A = 1/4$ are shown in Fig. 16). For larger forcing amplitudes, the profile becomes increasingly asymmetrical about $Y = 1$. Indeed, with the boundary conditions used, the system no longer satisfies the constraint $\int_0^{2\pi} Y dx = 1$, and so the fluid volume underneath the swimmer is not conserved, implying an outgoing flux. The physical significance of this result is obscured by the fact that we do not consider the flow dynamics ahead or behind the ends of the swimmer; to avoid such issues and to facilitate a faster exploration of some of the main features of the problem, we now focus on the low-amplitude limit.

5.2 Low-amplitude results

When $A \ll 1$, the fluid evolution equation can be linearised: $Y = 1 + \eta(x, t)$, $|\eta| \ll 1$, with

$$\eta_t = \frac{1}{12} p_{xx}, \quad p = D\eta_{xxxx} + A \sin k(x + t). \quad (5.2)$$

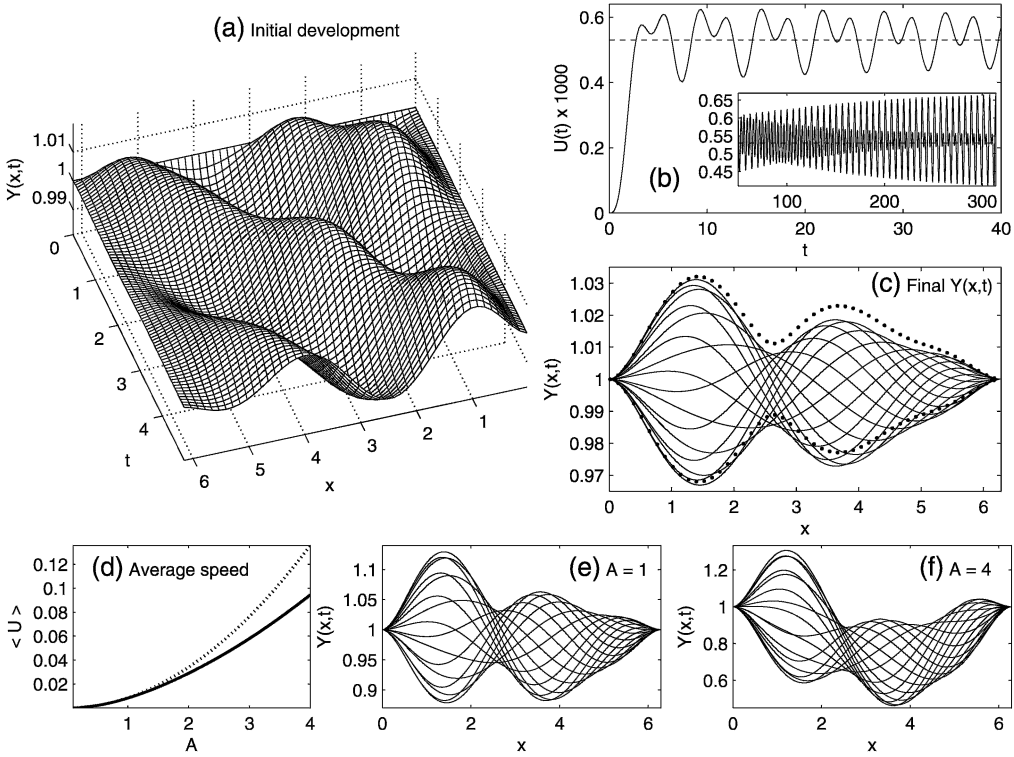


Fig. 16 Initial-value problem for a swimmer clamped at its head and tail, forced with $A = 1/4$ and $k = 1$; $D = M = 1$. Panel (a) shows the initial evolution of the swimmer profile, $Y(x, t)$, as a surface above the (x, t) -plane. Panel (b) shows the speed, $U(t)$, with an inset indicating the long-time behaviour. Panel (c) shows 16 snapshots during the cycle of the periodic state to which the solution eventually converges; the dots illustrate the envelope expecting from low-amplitude theory. Panel (d) shows the results of a suite of initial-value problems in which the final, average swimming speed, $\langle U \rangle$, was computed as a function of the forcing amplitude, A ; the dotted line shows the prediction of low-amplitude theory. Panels (e) and (f) show snapshots of periodic states with $A = 1$ and 4

The periodic solution of these equations can be formally written as

$$\eta = \frac{12kA \cos k(x+t)}{(144 + D^2k^{10})} - \frac{Dk^6 A \sin k(x+t)}{(144 + D^2k^{10})} + A \sum_{j=1}^{12} a_j e^{m_j x} \left(\cos kt + \frac{Dm_j^6}{12k} \sin kt \right), \quad (5.3)$$

where

$$m_j = \left(\frac{12k}{D} \right)^{1/6} e^{i\pi(2j-1)/12}, \quad (5.4)$$

and the coefficients of the homogeneous part a_j are determined by applying the specific boundary conditions (and depend on k and D). This form illustrates how the solution is a mix of standing and

propagating waves and can be fed into the right-hand side of

$$M\dot{U} = - \int_0^{2\pi} \left(U - \frac{1}{2} Y p_x \right) \frac{dx}{2\pi} \tag{5.5}$$

to furnish the swimming speed. Note that an average over the cycle of the final periodic state provides the mean speed

$$\langle U \rangle = \frac{k}{8\pi^2} \int_0^{2\pi} \int_0^{2\pi/k} \eta p_x dt dx, \tag{5.6}$$

which is independent of the swimmer's inertia. Given the linearity of (5.2), it follows that $\langle U \rangle \sim A^2$. Consequently, below, we quote only the scaled mean speeds $\langle U \rangle / A^2$ and omit further discussion of the effect of the forcing amplitude.

Figure 17 shows scaled speeds against forcing wave number at fixed bending stiffness ($D = 1$). For all four boundary conditions, the speeds are maximised for wave numbers near unity, a result also expected for a periodic swimmer, with speed $U/A^2 = 3k^2/(144 + D^2k^{10})$. The maximum arises because the effective strength of the forcing increases with k , but the stiffness of the swimmer penalises higher wave numbers. Finite swimmers also need not always swim forward: Fig. 17

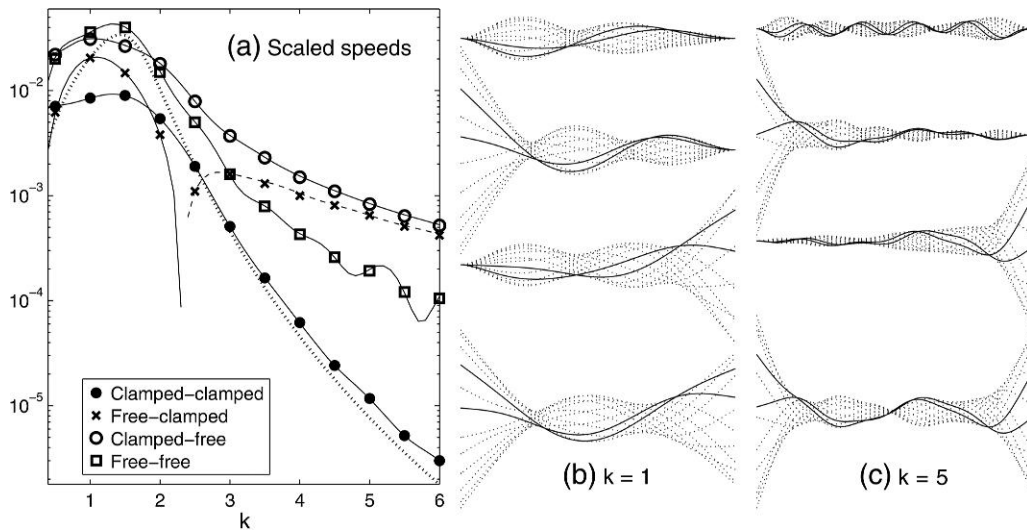


Fig. 17 Scaled swimming speeds, $\langle U \rangle / A^2$, for $D = 1$ and varying forcing wave number k . The left-hand panel shows the speeds computed for all four boundary conditions in (5.1); the periodic result, $U/A^2 = 3k^2/(144 + D^2k^{10})$, is shown by the dotted line. The speed for free clamped boundary conditions becomes negative for a certain k ; where it is negative, the scaled speed is plotted as a dashed line. The pictures on the right show snapshots of the swimmer profile at 12 instants during the swimming cycle for $k = 1$ and 5, with each row corresponding to the four different boundary conditions (the form of the profile at the ends reflects the relevant conditions). For each wave number, the profiles are shown with equivalent scales, except for the clamped-clamped case with $k = 5$, which is scaled additionally by a factor of three

illustrates how the swimmer that is free at $x = 0$ but clamped at $x = 2\pi$ actually moves backward when k is sufficiently large (that is, it moves in the same direction as the waves propagate).

For large wave number and low bending stiffness (see Fig. 18), the swimmer profile over the bulk of the body begins to resemble a periodic swimmer. Boundary layers emerge at the ends of the swimmer over which the solution adjusts to satisfy the relevant boundary conditions. However, as is evident in Fig. 18, the boundary layer and interior solutions are largely independent of one another: the solutions over the bulk are similar for all four boundary condition combinations, and each boundary layer solution is independent of the condition at the other end. The boundary layers remain pronounced even as $D \rightarrow 0$, to the degree that the mean swimming speed does not appear to converge to the corresponding periodic value, which might otherwise be expected (see Fig. 19).

At large bending stiffness, the swimmer is unable to significantly flex under the forcing, furnishing profiles with relatively low-amplitude and mild spatial oscillations (see Fig. 19). For $D \gg 1$, the homogeneous solutions in (5.3) reduce to a cubic polynomial in x and the mean speed can be shown to scale with D^{-2} (see Fig. 19). Different behaviour arises when both ends are free: in this instance, a much stronger rigid oscillation of the entire swimmer emerges. For example, if k is an integer, the form is approximately

$$Y \sim -\frac{15}{\pi^4 k^2} (x - \pi) \sin kt. \quad (5.7)$$

As this leading-order motion is reversible, it does not generate any net swimming; forward motion is controlled by the higher-order flexing of the swimmer, and the speed remains of order D^{-2} (see Fig. 19).

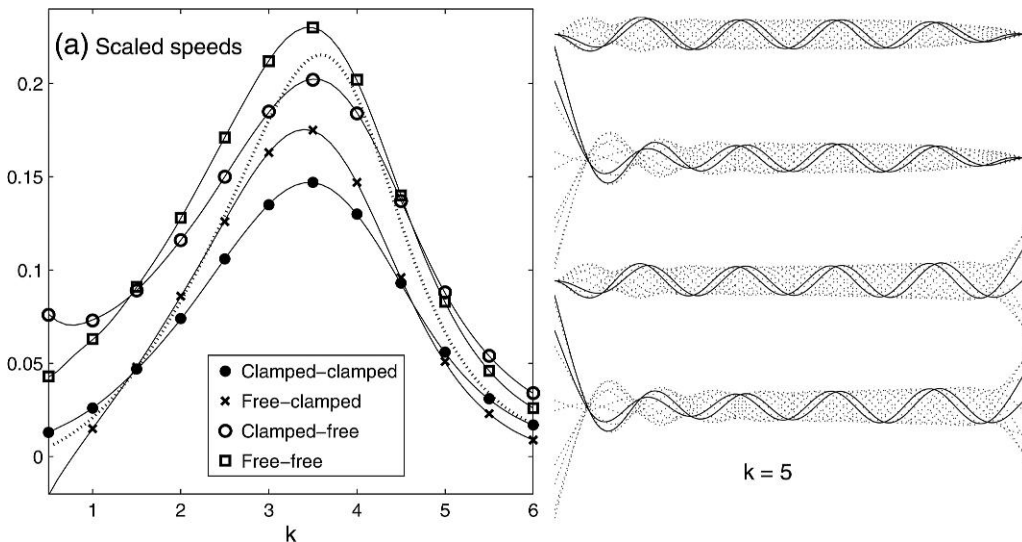


Fig. 18 Scaled speeds, $\langle U \rangle / A^2$, for $D = 10^{-3}$ and varying k are shown in the left-hand panel for each of the boundary conditions in (5.1). The dotted curve shows the periodic result. The snapshots on the right show 12 instants of the swimming cycle with $k = 5$ for each set of boundary conditions

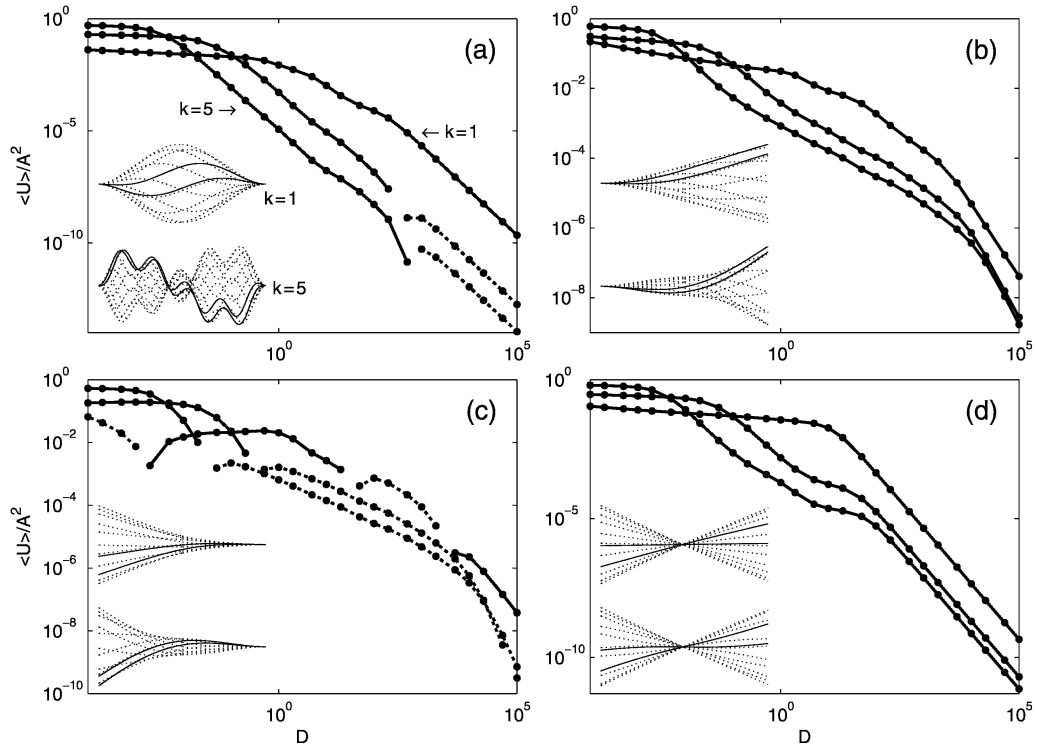


Fig. 19 Scaled speeds for varying D and $k = 1, 3$ and 5 . Panels (a)–(d) correspond to the four boundary conditions in (5.1) (the speeds for $k = 1$ are lowest at small D but highest at large D for each case). Lines are dashed where speeds are negative. The insets show 12 snapshots of the profile during the swimming cycles for $k = 1$ and $k = 5$ at $D = 10^3$

6. Conclusions

In Taylor’s model of a swimming microorganism, sinusoidal waves of low amplitude are sent down the length of a flexible sheet, propelling the object forward. Katz (2) took this model one step further, bringing the swimmer into the vicinity of a plane wall and allowing wave motions of higher amplitude, but still prescribed shape. Here, we have allowed the wave motions to be determined self-consistently by modelling the swimmer as an elastic filament bending under the action of an imposed force that propagates in a wave-like fashion along its length. Moreover, we have also filled the gap between the swimmer and the wall with complex fluid and explored how certain non-Newtonian effects influence the dynamics.

Had we fixed the profile of the wave that propagates down the swimmer, then we would have found that the swimming speed increases monotonically with forcing amplitude until the swimmer actually touches the wall. Of course, this situation is physically unrealistic, as the lubrication forces required to bring the surfaces into contact demand an unrealistically large forcing amplitude. Instead, by allowing the wave profile to be set by the solid mechanics of an elastic swimmer, we have seen that the swimming speed actually reaches a maximum and then decreases, as the forcing

amplitude is raised. The speed ultimately decreases in this situation because at the higher amplitudes, the swimmer is forced to press closer to the wall, which heightens the viscous resistance. Although there may be a biological need for the swimmer to gain a close proximity to the wall, if optimising the speed is the only requirement, then this selects a specific forcing amplitude. However, we have also prescribed the spatial pattern of the imposed forcing, and the existence of a preferred swimming speed and forcing amplitude suggests an interesting problem in optimal control if one is further allowed to shape the forcing pattern arbitrarily.

Our main results for swimmers in non-Newtonian fluid concern the case when the fluid has a yield stress. We have found that the forcing on the swimmer must exceed two thresholds before it begins its forward motion. Below the lower threshold, the forcing on the swimmer is unable to create any transverse motion whatsoever. But even when this threshold is exceeded, and waves are propagated down the swimmer, there is still no forward progress because yielding occurs only locally underneath each wave and rigid plugs persist in between that hold the swimmer in place. Only once we reach the second threshold, when the swimming action forces the fluid layer to yield everywhere, can forward motion occur. Both the flow underneath the swimmer and its shape are also strongly affected by the yield stress: a propagating pattern of plug-like velocity fields accompanies the wave travelling along the swimmer, and whenever the plugs touch the swimmer, the profile becomes flattened. Future studies of locomotive strategies adopted by real organisms may place these results in context by highlighting how the fluid environment influences the swimmer.

Finally, we presented a brief study of the effect of the head and tail of the swimmer by considering non-periodic, flexing sheets of finite length. For this situation, the swimming dynamics depends sensitively on the detailed boundary conditions at the head and tail, and there is no obvious optimal choice over the entire range of physical parameter values. More curiously, for certain swimming configurations, waves propagating down the sheet actually propel the swimmer backward.

Acknowledgement

We thank L. Fauci for discussions.

References

1. G. I. Taylor, Analysis of the swimming of microscopic organisms, *Proc. R. Soc. A* **209** (1951) 447–461.
2. D. F. Katz, On the propulsion of micro-organisms near solid boundaries, *J. Fluid Mech.* **64** (1974) 33–49.
3. J. Lighthill, *Mathematical Biofluidynamics* (SIAM, Philadelphia, PA 1975).
4. E. Lauga and T. R. Powers, The hydrodynamics of swimming microorganisms, *Rep. Prog. Phys.* **72** (2009) 096601.
5. B. Alberts, A. Johnson, J. Lewis, M. Raff, K. Roberts and P. Walter, *Molecular Biology of the Cell* (Garland Science, New York 2007).
6. D. F. Katz, R. N. Mills and T. R. Pritchett, The movement of human spermatozoa in cervical mucus, *J. Reprod. Fertil.* **53** (1978) 259–265.
7. D. F. Katz, T. D. Bloom and R. H. Bondurant, Movement of bull spermatozoa in cervical mucus, *Biol. Reprod.* **25** (1981) 931–937.
8. D. P. Wolf, L. Blasco, M. A. Khan and M. Litt, Human cervical mucus. I. Rheologic characteristics, *Fertil. Steril.* **28** (1977) 41–46.

9. D. P. Wolf, L. Blasco, M. A. Khan and M. Litt, Human cervical mucus. II. Changes in viscoelasticity during the ovulatory menstrual cycle, *ibid.* **28** (1977) 47–52.
10. M. Denny, The role of gastropod pedal mucus in locomotion, *Nature* **285** (1980) 160–161.
11. M. W. Denny, A quantitative model for the adhesive locomotion of the terrestrial slug, *ariolimax-columbianus*, *J. Exp. Biol.* **91** (1981) 195.
12. L. J. Fauci and A. McDonald, Sperm motility in the presence of boundaries, *Bull. Math. Biol.* **57** (1995) 679–699.
13. G. R. Fulford, D. F. Katz and R. L. Powell, Swimming of spermatozoa in a linear viscoelastic fluid, *Biorheology* **35** (1998) 295–309.
14. E. Lauga, Propulsion in a viscoelastic fluid, *Phys. Fluids* **19** (2007) 083104.
15. J. M. Skotheim and L. Mahadevan, Soft lubrication: the elastohydrodynamics of nonconforming and conforming contacts, *ibid.* **17** (2005) 092101.
16. S. J. Weekley, S. L. Waters and O. E. Jensen, Transient elastohydrodynamic drag on a particle moving near a deformable wall, *Q. Jl Mech. Appl. Math.* **59** (2006) 277–300.
17. Y. Jiao, S. Gorb and M. Scherge, Adhesion measured on the attachment pads of tettigonia viridissima (orthoptera, insecta), *J. Exp. Biol.* **203** (2000) 1887–1895.
18. S. N. Gorb, Biological attachment devices: exploring nature’s diversity for biomimetics, *Philos. Trans. R. Soc. A* **366** (2008) 1557–1574.
19. O. Pinkus and B. Sternlicht, *Theory of Hydrodynamic Lubrication* (McGraw-Hill, New York 1961).
20. B. Chan, N. J. Balmforth and A. E. Hosoi, Building a better snail: lubrication and adhesive locomotion, *Phys. Fluids* **17** (2005) 113101.
21. J. Wilkening and A. E. Hosoi, Shape optimization of a sheet swimming over a thin liquid layer, *J. Fluid Mech.* **601** (2008) 25–61.
22. T. K. Chaudhury, On swimming in a visco-elastic liquid, *ibid.* **95** (1979) 189–197.
23. L. Fauci and R. Dillon, Biofluidmechanics of reproduction, *Annu. Rev. Fluid. Mech.* **38** (2006) 371–394.
24. H. C. Fu, T. R. Powers and C. W. Wolgemuth, Theory of swimming filaments in viscoelastic media, *Phys. Rev. Lett.* **99** (2007) 258101.
25. T. Normand and E. Lauga, Flapping motion and force generation in a viscoelastic fluid, *Phys. Rev. E* **78** (2008) 061907.
26. G. J. Elfring, O. S. Pak and E. Lauga, Two-dimensional flagellar synchronization in viscoelastic fluids, *J. Fluid Mech.* **646** (2010) 505–515.
27. J. Teran, L. Fauci and M. Shelley, Peristaltic pumping and irreversibility of a Stokesian viscoelastic fluid, *Phys. Fluids* **20** (2008) 073101.
28. J. Teran, L. Fauci and M. Shelley, Viscoelastic fluid response can increase the speed and efficiency of a free swimmer, *Phys. Rev. Lett.* **104** (2010) 038101.
29. K. E. Machin, Wave propagation along flagella, *J. Exp. Biol.* **35** (1958) 796–806.
30. M. Argentina, J. Skotheim and L. Mahadevan, Settling and swimming of flexible fluid-lubricated foils, *Phys. Rev. Lett.* **99** (2007) 224503.
31. R. B. Bird, R. C. Armstrong and O. Hassager, *Dynamics of Polymeric Liquids* (Wiley, New York 1987).
32. R. H. Ewoldt, C. Clasen, A. E. Hosoi and G. H. McKinley, Rheological fingerprinting of gastropod pedal mucus and synthetic complex fluids for biomimicking adhesive locomotion, *Soft Matter* **3** (2007) 634–643.
33. N. J. Balmforth and C. J. Cawthorn, Contact in a viscous fluid: part I. A falling wedge, *J. Fluid Mech.* **646** (2010) 327–338.

34. E. Lauga and A. E. Hosoi, Tuning gastropod locomotion: modeling the influence of mucus rheology on the cost of crawling, *Phys. Fluids* **18** (2006) 113102.
35. N. J. Balmforth and R. V. Craster, A consistent thin-layer theory for Bingham plastics, *J. Non-Newtonian Fluid Mech.* **84** (1999) 65–81.
36. J. G. Oldroyd, On the formulation of rheological equations of state, *Proc. R. Soc. A* **200** (1950) 523–541.

APPENDIX A

Constitutive models

The Oldroyd-8 constitutive model is the most general constitutive model that respects the symmetries typical of fluid flow and the principle of material invariance and contains terms of quadratic nonlinear order in the deformation rates, yet remains linear in the stresses (31, 36). If τ denotes the deviatoric stress tensor, the law can be expressed in the *dimensional* form

$$\begin{aligned} \tau + \lambda_1 \overset{\nabla}{\tau} + \frac{1}{2} \mu_0 (\text{Tr } \tau) \dot{\gamma} - \frac{1}{2} \mu_1 (\tau \cdot \dot{\gamma} + \dot{\gamma} \cdot \tau) + \frac{1}{2} \nu_1 (\tau : \dot{\gamma}) \mathbf{I} \\ = \mu \left[\dot{\gamma} + \lambda_2 \overset{\nabla}{\dot{\gamma}} - \mu_2 \dot{\gamma} \cdot \dot{\gamma} + \frac{1}{2} \nu_2 (\dot{\gamma} : \dot{\gamma}) \mathbf{I} \right], \end{aligned} \quad (\text{A.1})$$

where μ is a polymeric viscosity, λ_1 and λ_2 are relaxation times, the deformation rates follow from the tensor

$$\dot{\gamma} = \nabla \mathbf{u} + (\nabla \mathbf{u})^T \equiv \begin{pmatrix} 2u_x & u_y + v_x \\ u_y + v_x & -2u_x \end{pmatrix} \quad (\text{A.2})$$

and the μ_j s and ν_j s are Oldroyd's other parameters. The upper convected derivative is

$$\overset{\nabla}{\tau} = \tau_t + u \tau_x + v \tau_y - [(\nabla \mathbf{u})^T \cdot \tau + \tau \cdot (\nabla \mathbf{u})]. \quad (\text{A.3})$$

For the slender flow geometry of our problem, and if ϵ denotes a typical aspect ratio,

$$\dot{\gamma} \sim \frac{c}{H} \begin{pmatrix} O(\epsilon) & O(1) \\ O(1) & O(\epsilon) \end{pmatrix}. \quad (\text{A.4})$$

Moreover, $\partial/\partial t$ and $\mathbf{u} \cdot \nabla$ are of order $\epsilon c/H$. Re-examining the constitutive law in light of these scalings, and assuming that all of $c^{-1} H(\lambda_j, \mu_j, \nu_j)$ remain of order one, implies that to leading order the stress components are given by the relations expected for steady-state, uni-directional shear flow in the x -direction:

$$\tau_{11} + (v_1 - \mu_1 - 2\lambda_1) u_y \tau_{12} = \mu (v_2 - \mu_2 - 2\lambda_2) u_y^2, \quad (\text{A.5})$$

$$2\tau_{12} + (\mu_0 - \mu_1 - 2\lambda_1) u_y \tau_{11} + (\mu_0 - \mu_1) u_y \tau_{22} = 2\mu u_y, \quad (\text{A.6})$$

$$\tau_{22} + (v_1 - \mu_1) u_y \tau_{12} = \mu (v_2 - \mu_2) u_y^2, \quad (\text{A.7})$$

where the numeric subscripts indicate the stress component. These equations are solved to yield the shear stress

$$\tau_{12} = \frac{\mu u_y (1 + \alpha u_y^2)}{1 + \beta u_y^2}, \quad (\text{A.8})$$

which is the only component that enters the leading-order force balance, and where

$$\alpha = \lambda_1 (v_2 - \mu_2) + \lambda_2 (\mu_0 - \mu_1) - (\mu_0 - \mu_1) (v_2 - \mu_2), \quad (\text{A.9})$$

$$\beta = \lambda_1 (v_1 + \mu_0 - 2\mu_1) - (\mu_0 - \mu_1) (v_1 - \mu_1). \quad (\text{A.10})$$

For the classical Oldroyd-B model, all the parameters ν_j and μ_j vanish, leaving $\alpha = \beta = 0$ and constant viscosity. A more interesting special case is the Johnson–Segalman model (31) for which $\alpha = -\lambda_1 \lambda_2 \xi (2 + \xi)$ and $\beta = -\lambda_1^2 \xi (2 + \xi)$, where ξ is another rheological parameter.

Note that the quasi-steady version of the non-Newtonian model emerges here because of our assumption that the Deborah numbers $H\lambda_j/c$ are of order one and in view of the lubrication scalings (unlike in papers by Lauga *et al.*). The viscoelastic model can be made richer in the slender limit if the scaled parameters $c^{-1}H(\lambda_j, \mu_j, \nu_j)$ are promoted to higher order in ϵ . The effects of time-dependent elasticity then appear in the problem, which unfortunately leads to a far less tractable partial differential form. Moreover, this upsets the leading-order force balance expressed in (2.1).

APPENDIX B

Flow profiles for the Bingham fluid

Given the pressure gradient and swimmer position, we compute various flow quantities as follows. Note that the case with $Y_+ > Y$ and $Y_- < 0$ can only arise for $U = 0$ and unyielded fluid. Also, given Y_{\pm} , we may compute the surface shear stresses from

$$\tau_0 = -\frac{1}{2}p_{\xi}(Y_- + Y_+), \quad \tau_1 = \frac{1}{2}p_{\xi}(2Y - Y_- - Y_+). \quad (\text{B.1})$$

A: $Y_{\pm} < 0$ ($p_{\xi} > 0$, $\tau_0 > B$, $\tau_1 > B$)

$$u = -U - yY_-p_{\xi} + \frac{1}{2}p_{\xi}y^2, \quad (\text{B.2})$$

$$Y_- = \frac{1}{2}Y - \frac{U}{Yp_{\xi}}, \quad Y_+ = Y_- + \frac{2B}{|p_{\xi}|}, \quad Q = Y - \frac{1}{2}U(1 - Y) - \frac{1}{12}p_{\xi}Y^3. \quad (\text{B.3})$$

B: $Y_- < 0 < Y_+ < Y$ ($p_{\xi} > 0$, $\tau_0 > B$, $\tau_1 > B$)

$$u = \begin{cases} -U, & 0 < y < Y_+, \\ -U + \frac{1}{2}p_{\xi}(y - Y_+)^2, & Y_+ < y < Y, \end{cases} \quad (\text{B.4})$$

$$Y_+ = Y - \sqrt{\frac{2U}{p_{\xi}}}, \quad Y_- = Y_+ - \frac{2B}{|p_{\xi}|}, \quad Q = Y - UY + \frac{1}{6}p_{\xi}(Y - Y_+)^3. \quad (\text{B.5})$$

C: $0 < Y_{\pm} < Y$ ($|\tau_0| > B$, $|\tau_1| > B$)

$$u = \begin{cases} u_p + \frac{1}{2}p_{\xi}(Y_- - y)^2, & 0 < y < Y_0, \\ u_p, & Y_- < y < Y_+, \\ u_p + \frac{1}{2}p_{\xi}(y - Y_+)^2, & Y_+ < y < Y, \end{cases} \quad (\text{B.6})$$

$$u_p = -\frac{1}{2}p_{\xi}Y_-^2 - U = -\frac{1}{2}p_{\xi}(Y - Y_+)^2, \quad (\text{B.7})$$

$$Y_+ = \frac{4B^2 + 2Up_{\xi} - Y^2p_{\xi}^2}{2|p_{\xi}|(2B - Y|p_{\xi}|)}, \quad Y_- = Y_+ - \frac{2B}{|p_{\xi}|}, \quad (\text{B.8})$$

$$Q = Y + \frac{1}{6}p_{\xi}[Y_-^3 + (Y - Y_+)^3 - 3Y(Y - Y_+)^2]. \quad (\text{B.9})$$

D: $0 < Y_- < Y < Y_+$ ($p_\xi < 0$, $\tau_0 > B$, $B > \tau_1 > -B$)

$$u = \begin{cases} \frac{1}{2}p_\xi(Y_- - y)^2, & 0 < y < Y_+, \\ 0, & Y_- < y < Y, \end{cases} \quad (\text{B.10})$$

$$Y_- = \sqrt{\frac{2U}{|p_\xi|}}, \quad Y_+ = Y_- + \frac{2B}{|p_\xi|}, \quad Q = Y + \frac{1}{6}p_\xi Y_-^3. \quad (\text{B.11})$$

E: $Y < Y_\pm$ ($p_\xi < 0$, $\tau_0 > B$, $\tau_1 > B$)

$$u = \left(U - \frac{1}{2}p_\xi Y^2 \right) \frac{y}{Y} + \frac{1}{2}p_\xi y^2 - U, \quad (\text{B.12})$$

$$Y_- = \frac{1}{2}Y - \frac{U}{Yp_\xi}, \quad Y_+ = Y_- + \frac{2B}{|p_\xi|}, \quad Q = Y - \frac{1}{2}UY - \frac{1}{12}p_\xi Y^3. \quad (\text{B.13})$$

For $U \rightarrow 0$, the following limits follow from the formulae above and coincide with the behaviour evident in Fig. 13.

For Case **B**, $Y_+ \rightarrow Y$ except for a narrow region close to $\zeta = \pi/2$ over which $p_\xi \sim O(U)$. Consequently, $Y_- \rightarrow Y - 2B/p_\xi$ and $Q \rightarrow Y$. Demanding that the flux be constant therefore implies that Y is almost constant, $Y \approx Y_*$. Moreover, the surface stresses become $\tau_1 \rightarrow +B$ and $\tau_0 \rightarrow B - Y_*p_\xi$.

For Case **D**, $Y_- \rightarrow 0$, except, once again, in a narrow region near $\zeta = \pi/2$ over which $p_\xi \sim O(U)$. This then implies that $Y_+ \rightarrow -2B/p_\xi$ and $Q \sim Y$. Thus, the swimmer profile must again become nearly constant, $Y \approx Y_*$, and the surface stresses reduce to $\tau_0 \rightarrow +B$ and $\tau_1 \rightarrow Y_*p_\xi + B$.